# Droplet Evolution and Refinement During Liquid–Liquid Decomposition of Zn-6 Wt Pct Bi Immiscible Alloy Under High Static Magnetic Fields

TIANXIANG ZHENG, YUNBO ZHONG, JIANG WANG, ZHONGMING REN, WEILI REN, ZUOSHENG LEI, FRANCOIS DEBRAY, ERIC BEAUGNON, and XICHENG WEI

*In situ* solidification experiments on Zn-6 wt pct Bi immiscible alloys were conducted to investigate the droplet evolution under high static magnetic fields (HSMFs). The results showed that a microstructure with extremely fine Bi-rich particles distributed in the matrix can be obtained under an HSMF of 29 T. The average diameter of the Bi-rich phase decreased with the increasing magnetic flux density. Stokes sedimentation disappeared when the HSMF was larger than 18 T. Starting at an HSMF of 18 T, Bi-rich droplets grew *via* pure diffusion in the liquid matrix. The HSMF decreased the spacing of the droplet arrays when the cooling rate ($R$) was approximately 1600 °C/min. The formation of a Zn-rich phase surrounded by a Bi-rich shell at HSMFs below 18 T, when $R$ was approximately 60 °C/min, was attributed to the thermoelectric magnetic force.

https://doi.org/10.1007/s11661-018-4638-8


## I. INTRODUCTION

IMMISCIBLE alloys, which are also known as monotectic alloys, have been of research interest for decades because of their excellent conductivity[1] and wear resistance.[2] However, in binary alloys, a solidified structure with segregation commonly forms under normal gravity conditions because of the Stokes sedimentation induced by the large density difference between the two elements. During liquid–liquid decomposition of immiscible alloys, the homogeneous melt separates into two immiscible liquid phases when the alloy is cooled to the immiscibility gap. The formed minority liquid droplets then settle or float because of the different specific densities of the liquid phases, and they migrate according to the temperature gradient. This droplet motion leads to severe phase segregation in the microstructure and even in the macrostructure of immiscible alloys. Many studies investigating the growth kinetics of liquid–liquid decomposition and suppression of phase segregation have been performed using a variety of external fields, such as microgravity fields,[3,4] centrifugal force fields,[5] electric fields,[6–8] and high static magnetic fields (HSMFs).[9,10] Yasuda *et al.*[9] found that the application of an HSMF can effectively decrease the sedimentation and coalescence of minority droplets. This implies that an HSMF induces microgravity conditions similar to those in aerospace experiments.[3,4] In addition, previous experimental results indicated that forced convective flow is effectively decreased under a suitable HSMF,[10] whereas the thermoelectric magnetic convection (TEMC) induced by the thermoelectric magnetic force (TEMF)[11,12] under a 4-T HSMF cannot be neglected. Simultaneously, changes in the particle size distribution were attributed to TEMC under a 4-T HSMF. Several reports[13–16] indicate that the application of an HSMF can affect the phase-transformation process by modifying the Gibbs free energy of Fe-C systems. Previous research has mostly focused on the effect of HSMFs on phase transformations, in which at least one phase was ferromagnetic. To date, there have been few studies on the phase transformation, droplet evolution, and growth behavior during solidification of diamagnetic immiscible alloys subjected to HSMFs. In addition, few researchers have focused on the ability of TEMC to modify the microstructure of an alloy during its bulk solidification process. Our previous results[17] showed that TEMC occurred during the bulk solidification of a Zn-6 wt pct

TIANXIANG ZHENG, YUNBO ZHONG, JIANG WANG, ZHONGMING REN, WEILI REN, and ZUOSHENG LEI are with the State Key Laboratory of Advanced Special Steels, Shanghai University, 149 Yanchang Road, Shanghai 200072, China. Contact e-mails: yunboz@staff.shu.edu.cn; ztx@shu.edu.cn FRANCOIS DEBRAY and ERIC BEAUGNON are with the LNCMI, CNRS/UJF/INSA/UPS, 38042 Grenoble, France. XICHENG WEI is with the School of Materials Science and Engineering, Shanghai University.

Manuscript submitted July 17, 2017.
Article published online May 21, 2018

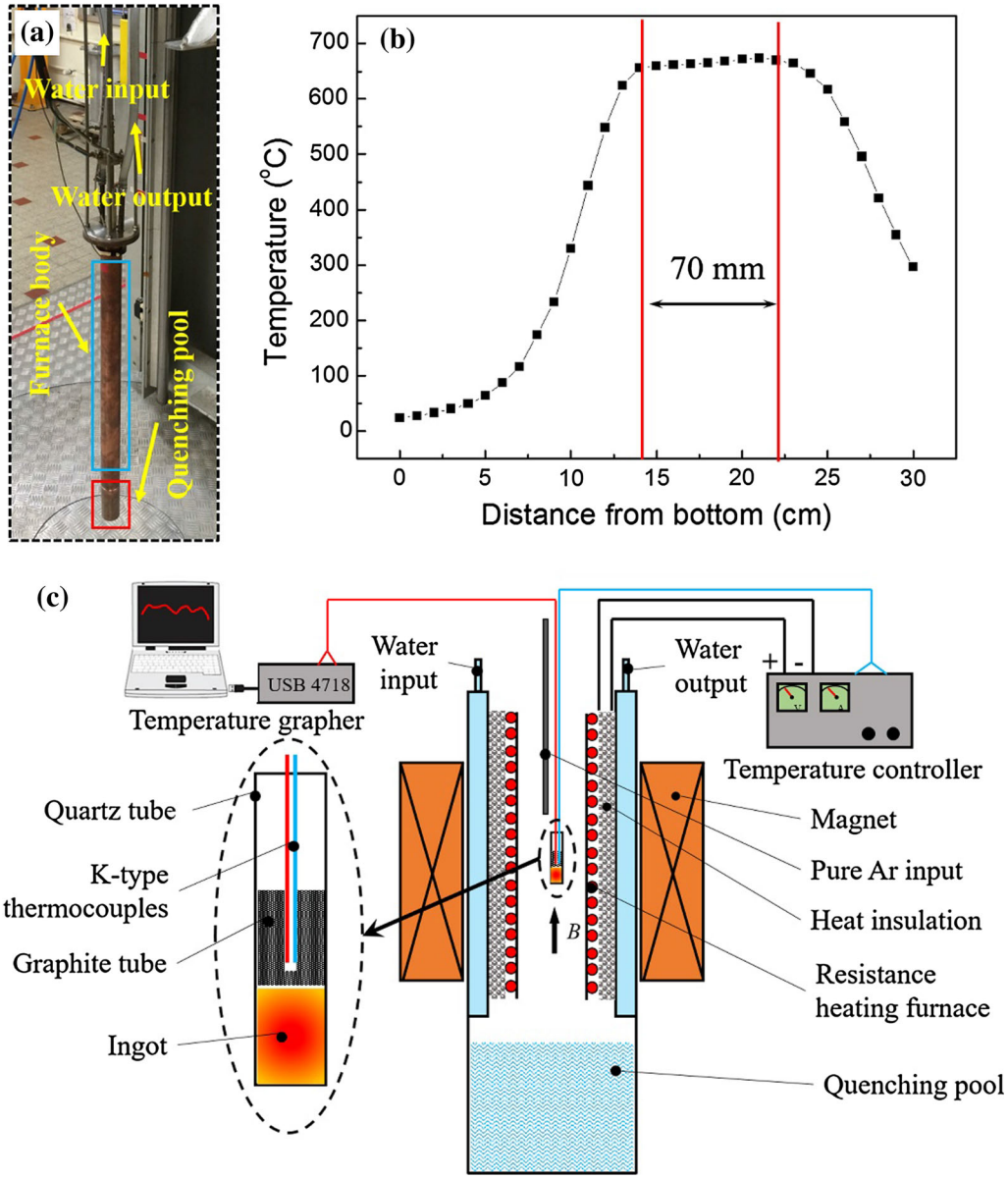


Fig. 1—(*a*) Photograph of the resistance-heating furnace. (*b*) Temperature profile of the furnace. (*c*) Schematic of the experimental setup.

Bi alloy and that it modified the distribution of the Bi-rich phase in a static transverse magnetic field.

In this study, a Zn-Bi alloy was used because of its low melting point and large immiscibility gap in the phase diagram. Our goal was to process a high-composition immiscible alloy without any phase segregation and then control the distribution of the minor phase by imposing an HSMF. We previously showed that Stokes sedimentation could be markedly suppressed by applying HSMFs of 17.4 and 29 T to a Zn-4 wt pct Bi alloy.[18] This alloy remained in the metastable region of the phase diagram during the solidification process. However, our previous work did not consider how the HSMFs affected the Stokes sedimentation process of a single droplet. Here, a rapid cooling (*in situ* quenching) method is used to shorten the sedimentation time of Bi droplets in the immiscibility gap. The current study provides valuable information on the phase transformation, droplet evolution, and growth behavior of a Zn-Bi immiscible alloy during liquid–liquid decomposition under HSMFs. TEMC induced by TEMF is also thought to occur during the bulk solidification process of the Zn-6 wt pct Bi immiscible alloy.

## II. EXPERIMENTAL

The Zn-6 wt pct Bi immiscible alloy was prepared using Zn particles (purity of 5N) and Bi particles (purity of 5N). The particle mixture with an appropriate ratio of components was placed in a quartz tube with an inner diameter and length of 8 and 150 mm, respectively. The mixture was heated to approximately

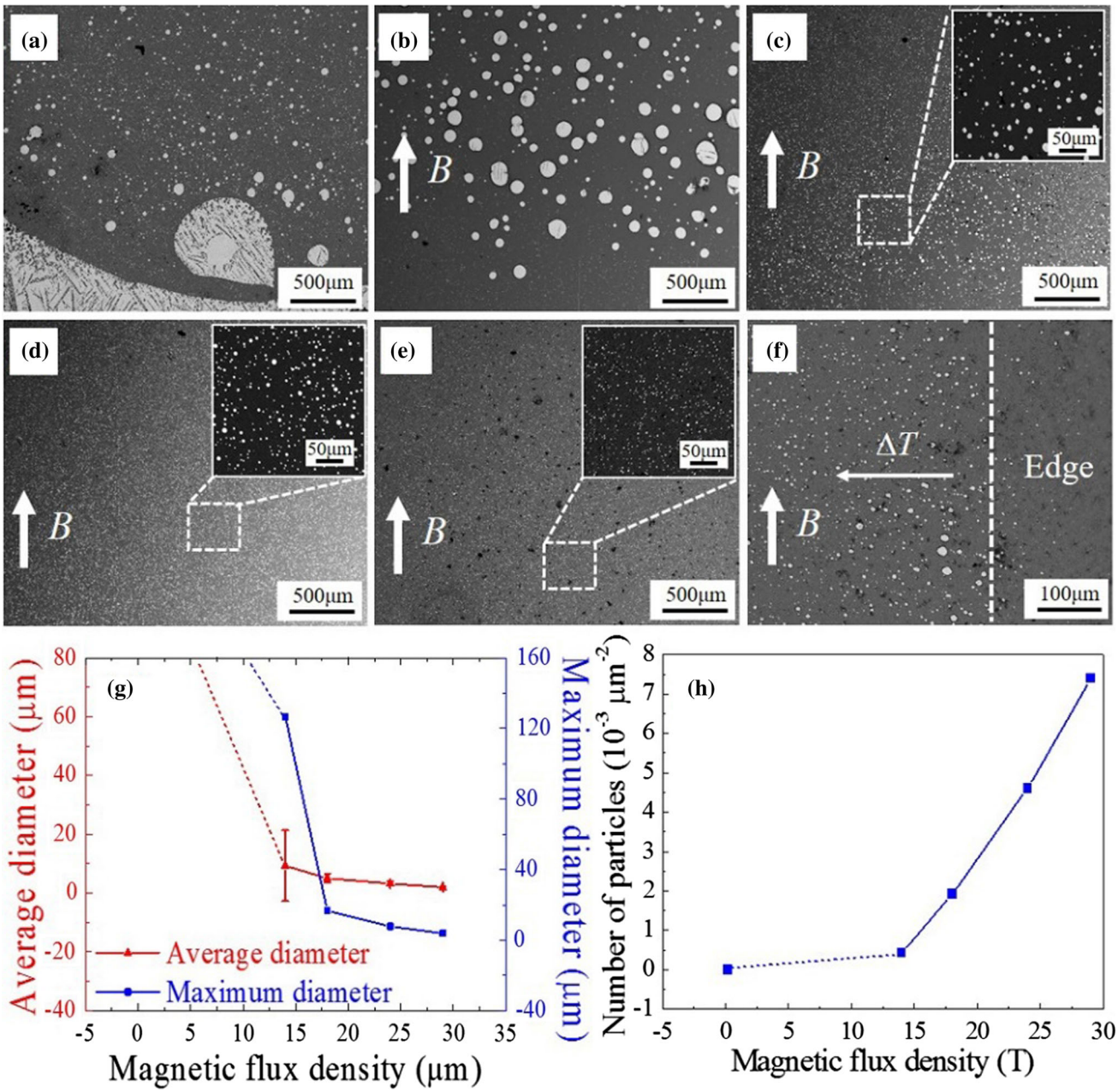


Fig. 2—Microstructure of Zn-6 wt pct Bi alloys solidified by *in situ* quenching ($R$ = 1600 °C/min) under HSMFs of (*a*) 0, (*b*) 14, (*c*) 18, (*d*) 24, and (*e*) 29 T. (*f*) Microstructure at the edge of the sample solidified at 29 T. (*g*) Dimensions of Bi-rich particles. (*h*) Number of particles per square micrometer. The red and blue dashed lines indicate the severe segregation of the $S_2$ phase in the alloy solidified without an HSMF; the diameter and the number of particles were very difficult to measure (Color figure online).

700 °C (above the critical temperature) using a vacuum electromagnetic induction heating furnace under the protection of highly pure Ar gas and then held at that temperature for 30 minutes. Then, the melt was naturally cooled to ambient temperature to obtain a cylindrical ingot with a diameter of 8 mm and length of 10 mm. The ingot was placed in the uniform heating region of an electric resistance-heating furnace inserted in the bore of the HSMF facility. The sample was heated to 700 °C and then held at this temperature for 60 minutes. The melt was then cooled to ambient temperature at different cooling rates $R$ (*in situ* quenching: $R$ = 1600 °C/min, natural cooling: $R$ = 60 °C/min) with or without a vertical HSMF. The HSMF was switched on after a holding time of 30 minutes and then switched off after the quenching process. The experiments with a 6-T HSMF were carried out using a superconducting magnet with a bore of an 80-mm diameter at room temperature at Shanghai University (Shanghai, China). The residual experiments were carried out using a Bitter resistance magnet with a bore with a 50-mm diameter at room temperature at LNCMI (Grenoble, France). A special electric resistance furnace designed to fit the 50-mm diameter

bore was used. The furnace mainly consisted of a copper tube ($\phi$ 49 mm) and molybdenum resistance wire ($\phi$ 1 mm). In addition, a water cooling system was included in the copper tube, and a copper quenching pool was attached to the bottom end of the tube. Figure 1(a) depicts the resistance-heating furnace with a circulating water cooling system and quenching pool at the bottom. Figure 1(b) shows the temperature profile in the furnace. The length (70 mm) marked in this profile represents the constant temperature region of the furnace in which the sample was positioned. Figure 1(c) presents a schematic diagram of the experimental setup. Two thermocouples were used in the experiment. One was used to control the sample temperature (blue line in Figure 1(c)), and the other was used to monitor the sample temperature (red line in Figure 1(c)). The phase diagram of Zn-Bi is shown in supplementary Figure 1.

The solidified samples were sectioned along the parallel and perpendicular directions to the direction of the HSMF and then polished mechanically. The microstructures and morphologies of the alloys were

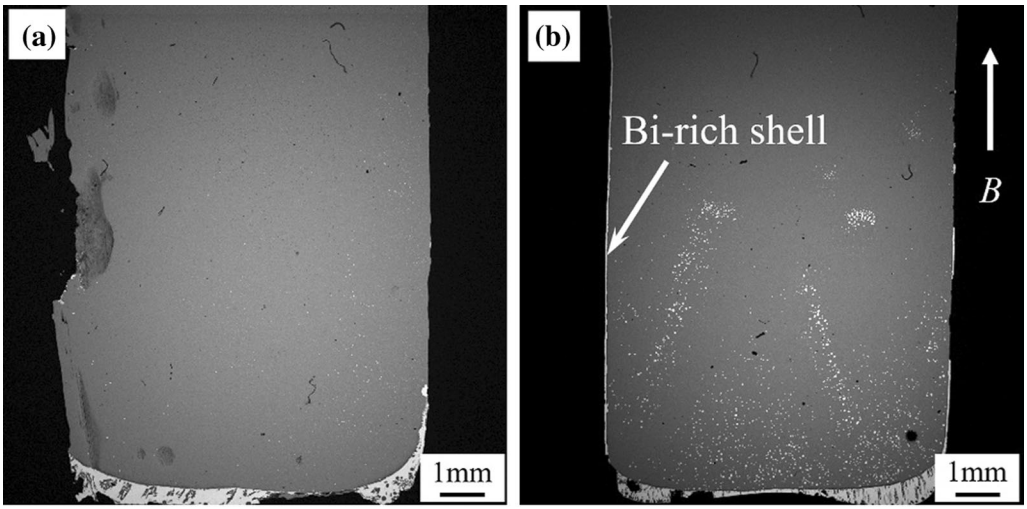


Fig. 3—Macrodistribution of the $S_2$ phase in Zn-6 wt pct Bi samples solidified by natural cooling (60 °C/min) at (*a*) 0 and (*b*) 18 T.

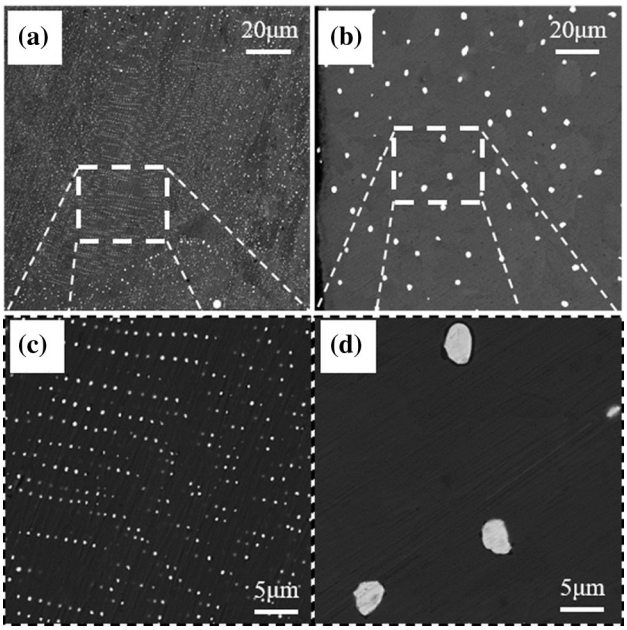


Fig. 4—Perpendicular microstructures in the left middle margin of Zn-6 wt pct Bi solidified without an HSMF with (*a*) *in situ* quenching ($R$ = 1600 °C/min) and (*b*) natural cooling ($R$ = 60 °C/min) (*c*) and (*d*) enlarged images.

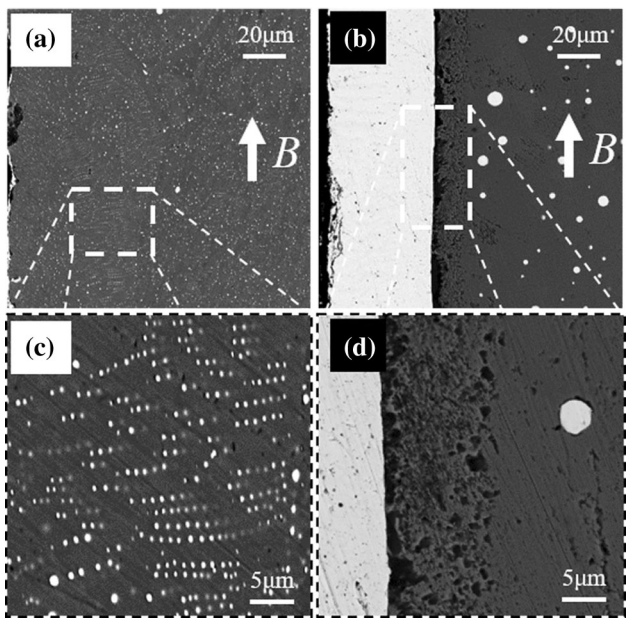


Fig. 5—Perpendicular microstructures in the left middle margin of Zn-6 wt pct Bi solidified under an 18-T HSMF. (*a*) *In situ* quenching ($R$ = 1600 °C/min) and (*b*) natural cooling ($R$ = 60 °C/min) (*c*) and (*d*) Enlarged images.

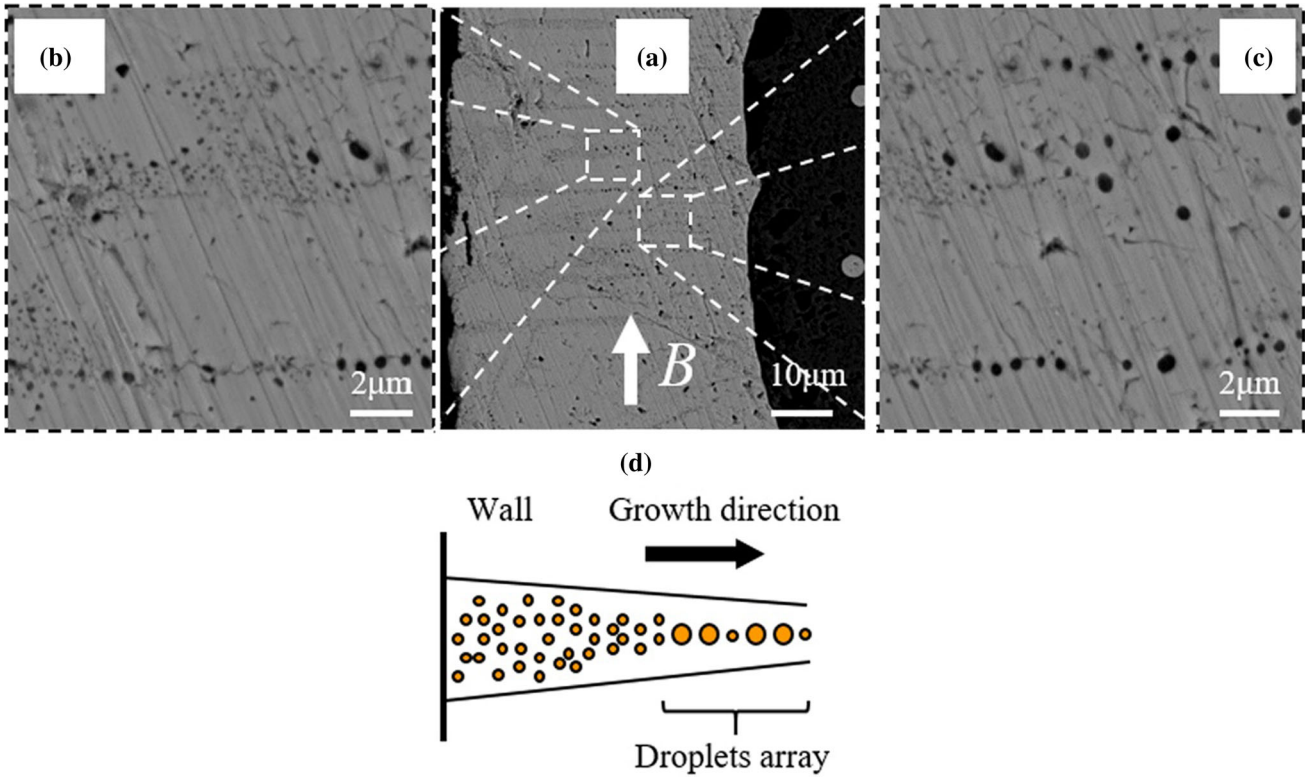


Fig. 6—Microstructural evolution of the $S_2$ shell surrounding the sample solidified under an 18-T HSMF ($R$ = 60 °C/min). (*a*) Parallel reaction bands close to the crucible wall. (*b*) Microstructure of the reaction band in the transition region. (*c*) Rayleigh-type microstructure at the tip of the reaction band. (*d*) Schematic diagram of the microstructural evolution process.

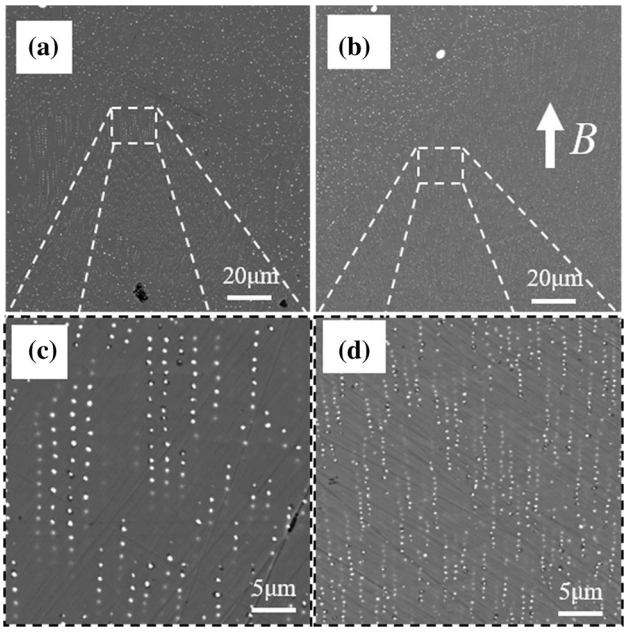


Fig. 7—Rayleigh-type microstructure in the bottom region of samples solidified at 1600 °C/min under HSMFs of: (*a*) 0 and (*b*) 18 T. (*c*) and (*d*) enlarged images.

characterized using the backscattered electron (BSE) imaging function of a scanning electron microscope (VEGA3 SBH-Easyprobe).

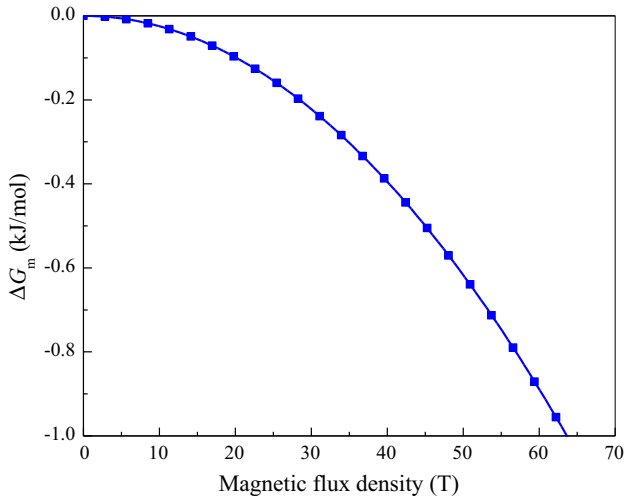


Fig. 8—Relationship between the magnetic Gibbs free energy per unit volume ($\Delta G_m$) and magnetic flux density ($B$).

## III. RESULTS

### A. *Effects of HSMFs on the Microstructure of the Zn-6 Wt Pct Bi Alloy*

Our previous study[18] revealed that a very small amount of the solid Bi-rich phase ($S_2$) aggregated at the bottom of the samples. Therefore, the region located approximately 2 to 3 mm from the bottom edge of the

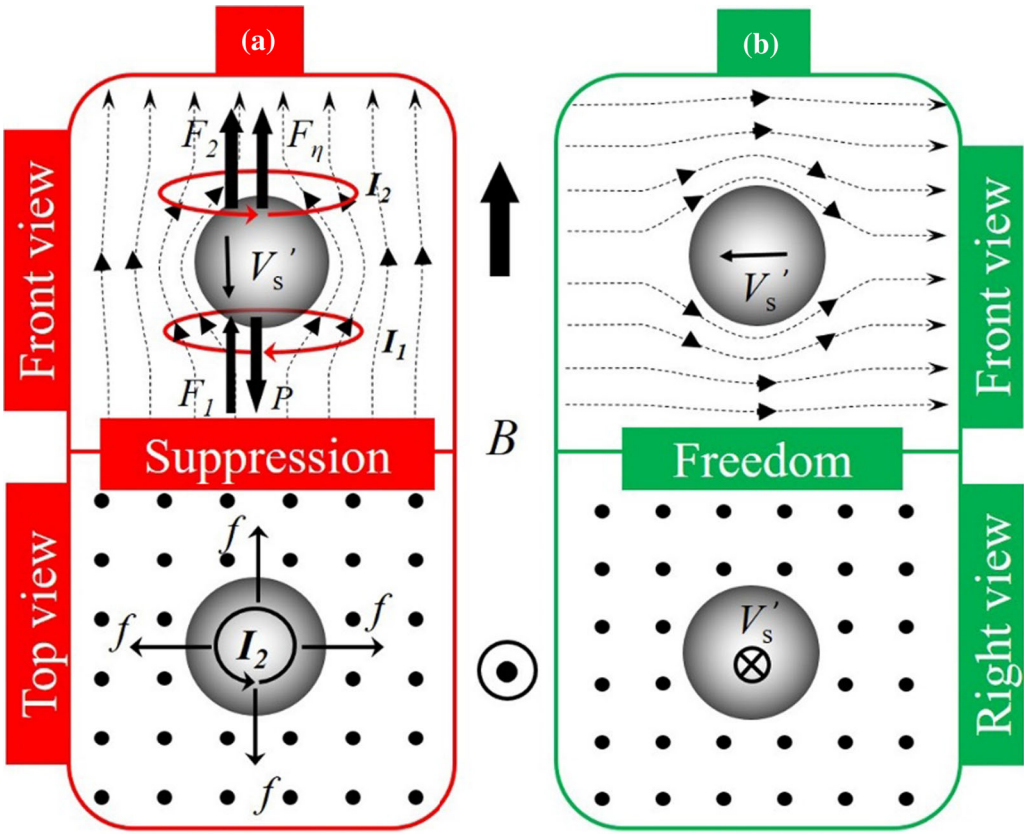


Fig. 9—Single droplet as it moves parallel and perpendicular to an HSMF: (*a*) $V_S' \parallel B$, movement is hindered by the HSMF; (*b*) $V_S' \perp B$, droplet moves freely in the liquid matrix. The dashed lines represent the flow pattern around the sinking $L_2$ droplet. Here, $V_S'$ is the velocity of the droplet in the melt under an HSMF.

sample along the central axis, which was photographed in this study, was considered representative to estimate the segregation in each ingot. Figure 2 shows the BSE images of the longitudinal microstructures at the bottom of the Zn-6 wt pct Bi samples solidified at $R = 1600$ °C/min with and without an HSMF. The solid Zn-rich phase ($S_1$) appears gray, whereas the $S_2$ phase is white. A layered microstructure is visible in the sample solidified without an HSMF (Figure 2(a)). As the magnetic flux density ($B$) was increased from 14 to 29 T, the degree of segregation decreased dramatically (from Figures 2(b) through (e)). However, when the temperature difference ($\Delta T$) caused by the radial temperature gradient was large, slight segregation occurred at the edge of the sample solidified under a 29-T HSMF (Figure 2(f)). The average diameter ($d_a$) of the $S_2$ particles decreased to less than 10 $\mu$m when $B$ was greater than 18 T. However, the maximum diameter ($d_m$) of the particles remained greater than 10 $\mu$m until $B$ exceeded 24 T. The $d_m$ values were 7.79 and 3.8 $\mu$m at $B$ of 24 and 29 T, respectively (Figure 2(g)). The number of $S_2$ particles increased from $0.45 \times 10^{-3}$ to $7.4 \times 10^{-3}$ $\mu m^{-2}$ as $B$ rose from 14 to 29 T, as shown in Figure 2(h). Previous studies[19,20] indicated that droplets with a diameter of 1 $\mu$m are large enough to produce a substantial surface tension difference between the hot and cool parts, thus facilitating Marangoni migration. Stokes sedimentation occurs when the droplet diameter is greater than 10 $\mu$m. Thus, segregation occurred when $B$ was lower than 14 T because the average size of particles was larger than 10 $\mu$m in this case. Marangoni migration was the predominant factor leading to the segregation of the microstructure when $B$ exceeded 18 T.

### B. *Effects of Cooling Rate on Alloy Microstructure Under an 18-T HSMF*

Comparing the BSE images showing the macrostructure of the Zn-6 wt pct Bi sample solidified by natural cooling under 0 T with that solidified under 18 T (Figure 3) revealed an interesting phenomenon that has only been observed previously under microgravity conditions.[3,4] That is, for the sample solidified under an 18-T HSMF, $S_1$ was surrounded by $S_2$ to form a shell-type macrostructure. The thickness of the $S_2$ shell was uniform around $S_1$ on the left side of the sample, but it was discontinuous on the right side, as shown in Figure 3(b). In this experiment, an 18-T HSMF was applied during the solidification process, whereas low-gravity conditions were used in the reported studies.[3,4] This indicates that the application of HSMFs produced an experimental environment that was similar to that obtained under microgravity conditions.

To carry out an exhaustive investigation on the evolution process during solidification, the microstructure of the alloy samples near the quartz crucible was

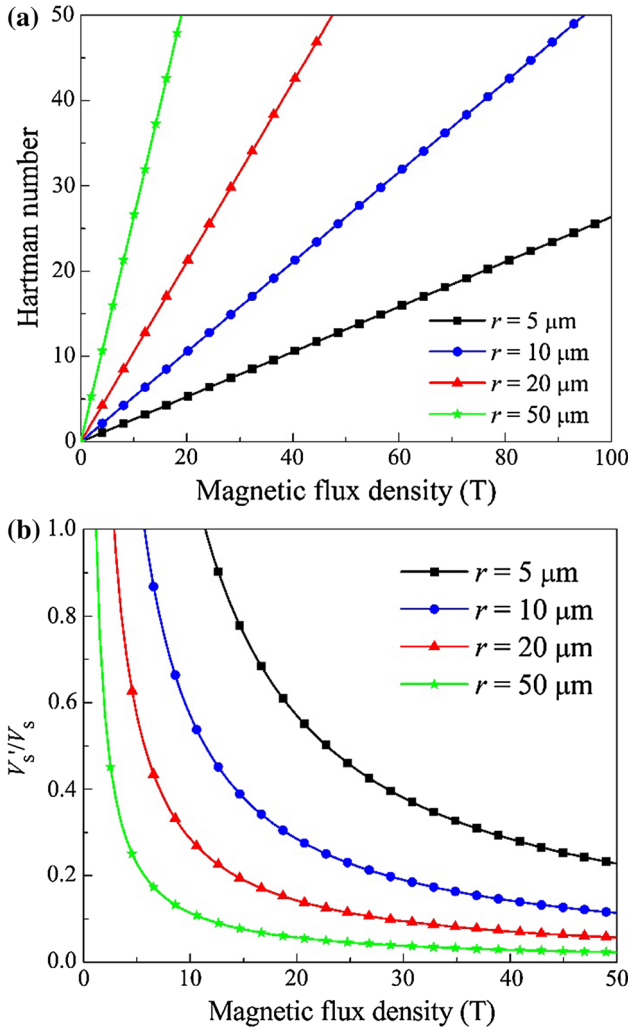


Fig. 10—(*a*) Relationship between the Hartman number and magnetic flux density (*B*). (*b*) Relationship between the ratio of $V_S'/V_S$ and *B*.

carefully studied. Figure 4 compares the samples solidified without an HSMF at different *R*. Some Rayleigh-type regular arrays of $S_2$ particles, which have only previously been observed in directional solidification experiments,[21–23] appeared in the region close to the crucible wall. The particle arrays extended along the radial direction to the central axis of the sample. The average spacing ($\lambda$) of the arrays was approximately 1.5 $\mu$m.

Figure 5(a) reveals that the sample solidified under an 18-T HSMF at 1600 °C/min has the same Rayleigh-type arrays of $S_2$ particles in the left middle margin. $\lambda$ of the particle arrays was 1.3 $\mu$m, which is smaller than that without an HSMF (1.5 $\mu$m). Comparing Figures 4(c) with 5(c) showed that the average length of the particle arrays in Figure 4(c) (13 $\mu$m) was longer than that of the particle arrays in Figure 5(c) (8 $\mu$m). Meanwhile, Figure 5(b) shows that a uniform $S_2$ shell with a thickness of 48.9 $\mu$m formed under an external HSMF. In addition, the $S_1$ phase near the $S_2$ shell was different from the inner $S_1$ phase. Many defects and an interface between $S_2$ and $S_1$ were found in this limited region. The reason for the formation of defects will be discussed below.

Figure 6 shows that some parallel reaction bands with a chain-like pattern existed near the crucible wall for the sample solidified under an 18-T HSMF with $R = 60$ °C/min. The thickness of each band decreased as the distance from the wall to the center increased (Figure 6(a)). Figure 6(b) illustrates the transient microstructure between the parallel reaction bands (Figure 6(a)) and Rayleigh-type microstructure (Figure 6(c)). The reaction bands turned into a Rayleigh-type microstructure similar to the microstructures shown in Figures 4(a) and 5(a).

Figure 7 shows the Rayleigh-type microstructure observed at the bottom regions of samples solidified at 1600 °C/min under HSMFs of 0 and 18 T. Based on the measured data, $\lambda$ of the particle arrays in the sample solidified under 0 T was 2.0 $\mu$m, which is larger than that of the sample solidified under 18 T (1.1 $\mu$m). The average length of the particle arrays shown in Figure 7(a) (15 $\mu$m) was longer than that in Figure 7(b) (5 $\mu$m). Thus, Rayleigh-type particle arrays appeared not only at the outer edge but also at the bottom region of the samples.

## IV. DISCUSSION

### A. *Effects of an HSMF on the Phase Transformation of Zn-Bi Alloy*

Based on the results in Figures 2(g) and (h), it was hypothesized that the nucleation process was affected by the HSMF. It is known that during the solidification process, Zn-6 wt pct Bi enters both the metastable and unstable regions of the Zn-Bi phase diagram.[10] The mixed liquid phase or mother liquid melt (L) then decomposes into a liquid Zn-rich matrix ($L_1$) and liquid Bi-rich phase ($L_2$) below the binodal line, not only through nucleation and growth in the metastable region but also by spinodal decomposition in the unstable region. The size of the metastable region is larger than that of the unstable region for the Zn-6 wt pct Bi alloy. Thus, the liquid–liquid decomposition occurs mainly through nucleation and growth in the metastable region. Naturally, there is an energy barrier to overcome during the nucleation stage of the $L_2$ droplets. Under an HSMF, a magnetic Gibbs free energy ($\Delta G_M = \Delta G_m \cdot V$, where $\Delta G_m$ is the magnetic Gibbs free energy per unit volume and $V$ is the volume of the droplet) is produced with the appearance of the $L_2$ droplets, and it acts as a driving force for phase transformation. $\Delta G_m$ equals $-\Delta\chi B^2/2\mu_0$,[24–26] where $\Delta\chi$ is the difference of magnetic susceptibility per volume between L and an $L_2$ droplet and $\mu_0$ is the permeability of vacuum and equals $4\pi \times 10^{-7}$ H/m. We assumed that L can be represented by the Zn melt and the $L_2$ droplet can be represented by Bi melt. Both liquid Zn and liquid Bi are known as abnormal diamagnetic phases with magnetic susceptibilities of about $-6.58\times10^{-7}$ (measured at 419 °C) and $-0.38\times10^{-7}$ (measured at 450 °C), respectively.[27–29]

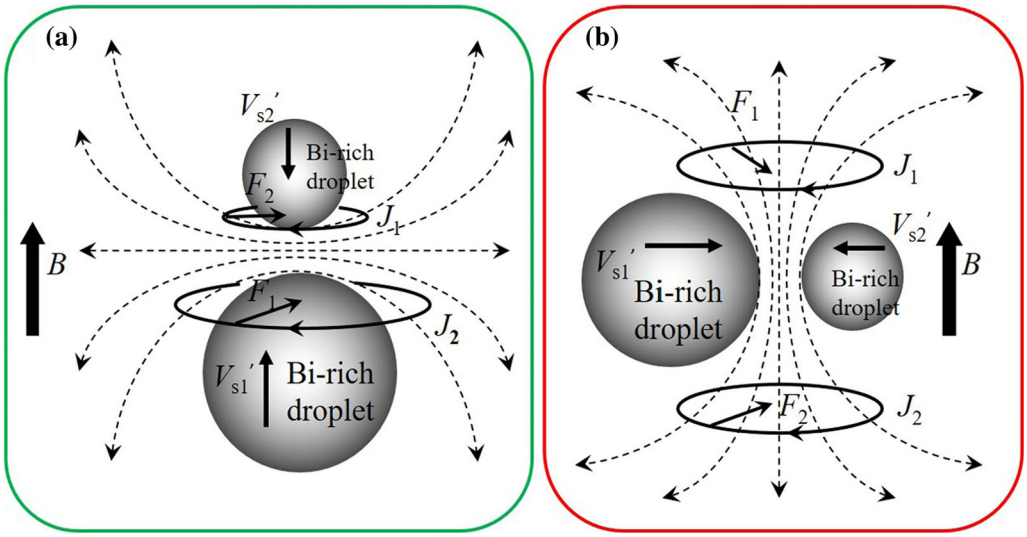


Fig. 11—Two droplets as they move parallel and perpendicular to the HSMF: (*a*) $V_{s1}'$ and $V_{s2}'$ // $B$ (*b*) $V_{s1}'$ and $V_{s2}' \perp B$. Here, $V_{s1}'$ and $V_{s2}'$ are the velocities of the two droplets in the melt under an HSMF.

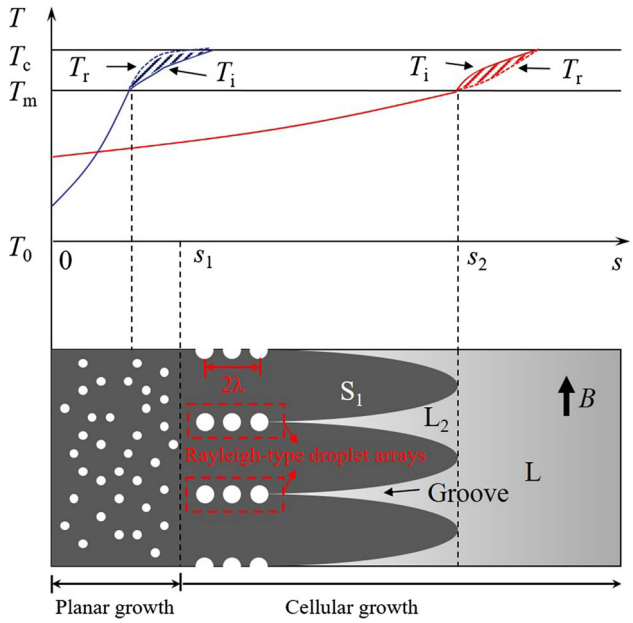


Fig. 12—Schematic of the growth process in a grain at the sample surface. $T_c$ and $T_m$ are the critical temperature and monotectic reaction temperature, respectively, and are shown in Supplementary Figure 1.

Then, $\Delta\chi$ was calculated to be $6.2\times10^{-7}$. $\Delta G_m$ decreases with increasing $B$, as shown in Figure 8. When $B$ is 29 T, $\Delta G_m$ is calculated to be about − 250 J/mol. However, this is much smaller than the thermal energy of 2.5 kJ/mol at room temperature. Therefore, the HSMF has little effect on the nucleation of $L_2$ droplets in the liquid matrix. That is, it can be deduced that the magnetohydrodynamic effect is the main reason for the refinement of $S_2$ particles in Figure 2(c) and magnetothermodynamic effect can be neglected under HSMFs of less than 29 T.

### B. *Effects of HSMFs on the Coalescence and Growth of Bi-Rich Droplets*

After the nucleation process, the $L_2$ droplets grow gradually. They are driven by the Marangoni motion when the droplet diameter ($d$) is less than 10 $\mu$m and by additional Stokes motion when $d$ exceeds 10 $\mu$m. In addition, the $L_2$ droplets tend to collide with each other to form larger droplets. If we assume that a single $L_2$ droplet ($d > 10$ $\mu$m) settled with a certain velocity at the bottom of the sample, the HSMF decreases the velocity to a constant value ($V_1$) through the induced Lorentz forces inside the $L_1$ melt, both at the front and back of the $L_2$ droplet (Figure 9(a)). The melt flow has horizontal components at the front and back of the $L_2$ droplet. The horizontal component of the melt flow and HSMF efficiently induce an eddy current; that is, clockwise and counterclockwise currents are induced at the front and back sides, respectively. Then, the electromotive forces ($F_1$ and $F_2$) induced by electromagnetic induction decrease the deformation of the melt and simultaneously slow the motion of the $L_2$ droplets. $F_1$ and $F_2$ are viscous resistances that can be analyzed in terms of the Hartmann number (Ha),[9,30] which can be written as

$$Ha = 2Br\sqrt{\sigma/\eta_1}, \qquad [1]$$

where $r$ is the radius of the $L_2$ droplet, and $\sigma$ and $\eta_1$ are the electrical conductivity and viscosity of $L_1$, respectively. If we assume that $L_1$ and $L_2$ are pure Zn and pure Bi, respectively, then the relationship between Ha and $B$ at the melting point of Zn (419.6 °C) can be calculated (Figure 10(a)). In the melt, the additional viscous resistance ($F_\eta$) without an HSMF can be defined by

$$F_\eta = 6\pi r\eta_1 V_s \frac{2\eta_1 + 3\eta_2}{3\eta_1 + 3\eta_2}, \qquad [2]$$

where $V_s$ is the moving velocity of the $L_2$ droplet in the melt without an HSMF and $\eta_2$ is the viscosity of

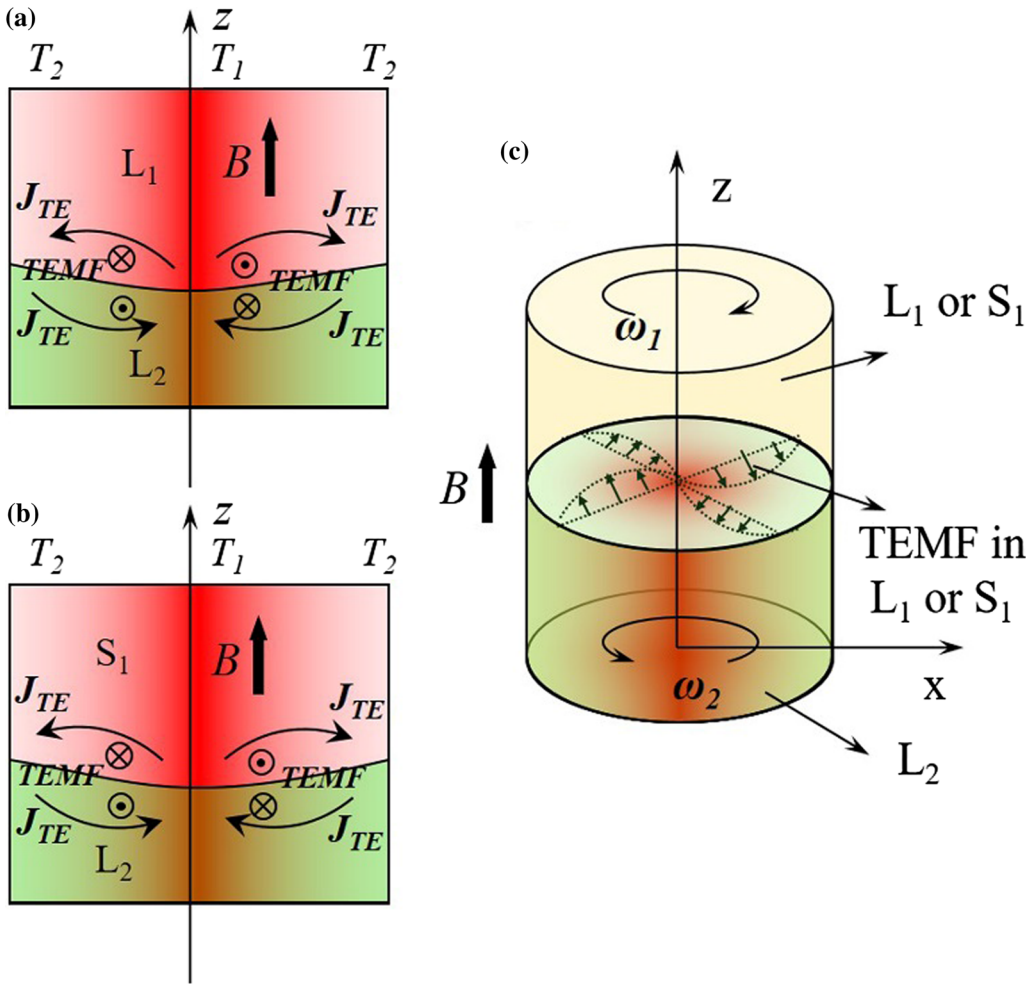


Fig. 13—Schematic of the formation of thermoelectric current ($J_{TE}$) and thermoelectric magnetic force (TEMF) at the $L_1$–$L_2$ and $S_1$–$L_2$ interfaces. $J_{TE}$ induced by radial temperature ($T_1 > T_2$) for the (*a*) $L_1$–$L_2$ and (*b*) $S_1$–$L_2$ interfaces; (*c*) TEMF generated by the interaction between $J_{TE}$ and the external HSMF.

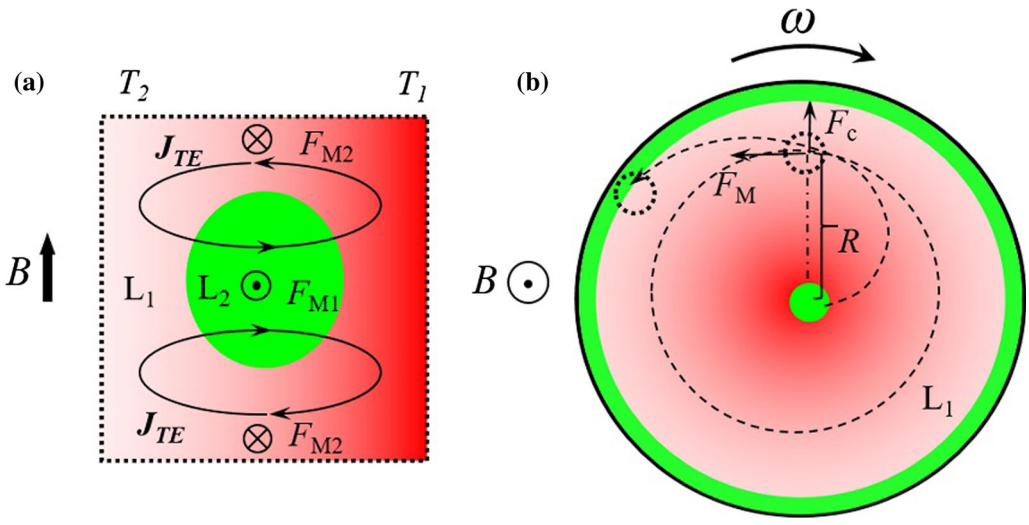


Fig. 14—Schematic of the thermoelectric magnetic force (TEMF) inside the immiscible melt: (*a*) front view of the interaction between the thermoelectric current and magnetic flux density ($B$) with a radial temperature gradient ($T_1 > T_2$) and (*b*) top view of the migration of an $L_2$ droplet inside the immiscible melt. $F_{M1}$ is the TEMF in the $L_1$ melt and $F_{M2}$ is the TEMF in the $L_2$ droplet.

the $L_2$ droplet. The viscous resistance under the effect of an HSMF ($F_\eta'$) can be expressed as[9,30,31]

$$F'_\eta = 6\pi r\eta_1 V'_s \frac{2\eta_1 + 3\eta_2}{3\eta_1 + 3\eta_2}\frac{\mathrm{Ha}}{3}[1 + \mathrm{O}(\mathrm{Ha})] \quad (\mathrm{Ha} > 1) \quad [3]$$

We can use Eqs. [2] and [3] to determine the terminal velocity of a droplet falling vertically in the melt. In this case, forces $F_\eta$ and $F_\eta'$ compensate for the gravity-induced buoyancy force $P$, which can be expressed as

$$P = 4\pi r^3 g(\rho_2 - \rho_1)/3, \quad [4]$$

where $\rho_1$ and $\rho_2$ are the densities of $L_1$ and $L_2$, respectively; and $g$ is the acceleration caused by gravity. The movement of an $L_2$ droplet becomes stable after balancing these forces. This state is described as below:

$$\begin{aligned}\frac{4}{3}\pi r^3 g(\rho_2 - \rho_1) &= 6\pi r\eta_1 V_s \frac{2\eta_1 + 3\eta_2}{3\eta_1 + 3\eta_2} \\ &= 6\pi r\eta_1 V'_s \frac{2\eta_1 + 3\eta_2}{3\eta_1 + 3\eta_2}\frac{\mathrm{Ha}}{3}[1 + \mathrm{O}(\mathrm{Ha})]\end{aligned} \quad [5]$$

Then, we can obtain the ratio $V_S'/V_S$, which is used to quantify the effect of the HSMF and has been described in our previous work.[18]

$$\frac{V'_s}{V_s} = \frac{1}{Br}\sqrt{\frac{\eta_1}{\sigma}} \quad [6]$$

The physical parameters used in the equations can also be found in Reference 18. Then, we can obtain the relationship between $V_S'/V_S$ and $B$, as seen in Figure 10(b). The suppression of the Stokes sedimentation can be expressed by $\delta_S = (V_S - V_S')/V_S \times 100$ pct. For an $L_2$ droplet with a radius of 10 $\mu$m, $\delta_S$ values are approximately 50, 70, and 80 pct when $B$ values are 10, 20, and 30 T, respectively. The $L_2$ droplet in the $L_1$ melt also displays another type of motion, as shown in Figure 9(b). In this case, the direction of motion of the $L_2$ droplet is perpendicular to the HSMF; therefore, no eddy currents are induced on either the front or back side of the $L_2$ droplet along its moving direction. The movement of the $L_2$ droplet is free in the HSMF. The Marangoni migration of the $L_2$ droplets occurred when there was a large temperature gradient along the radial direction of the sample (perpendicular to the direction of the HSMF). This led to slight segregation at the edge of the sample (Figure 2(f)).

The coalescence of droplets under an HSMF can also be explained by considering the melt flow around the immiscible droplets. Figures 11(a) and (b) show the coalescence of two $L_2$ droplets in the vertical and horizontal directions, respectively. In the case of coalescence of two droplets moving parallel to the HSMF, the $L_1$ melt is ejected from the gap between the two $L_2$ droplets. The melt flow of $L_1$ to the top part of the upper droplet and bottom part of the lower droplet is also induced. The electromagnetic induction caused by the flow pattern around the droplets is equal to that shown in Figure 9(a). The eddy currents ($J_1$ and $J_2$) induced by the melt flow around the droplets are represented by solid black lines. Lorentz forces induced by the eddy current and HSMF, which are shown in Figure 11(a), act as a braking force to prevent the collision between the two $L_2$ droplets. Thus, the HSMF lowers the coalescence rate in the direction parallel to the HSMF. The situation shown in Figure 11(b) is the same as that observed in Figure 11(a). In this case, the horizontal component of the $L_1$ melt flow at the top part of the two droplets induces a clockwise current ($J_1$). The $L_1$ melt flow at the bottom part of the two droplets also induces a clockwise current ($J_2$). The HSMF and clockwise currents induce Lorentz forces that resist the $L_1$ melt flow from the gap to the back of the droplets. The coalescence of the $L_2$ droplets in the horizontal direction is also suppressed by the HSMF. Thus, coalescence in both the vertical and horizontal directions is hindered by applying an HSMF. This means that the Marangoni motion at the edge of the sample can also be decreased, as we described in our previous work.[18]

The measured data showed that the radius of the $L_2$ droplet was smaller than 10 $\mu$m when $B \geq 18$ T, which resulted in no Stokes sedimentation, and thus the growth process was no longer controlled by the Stokes sedimentation. In this situation, the movement of the $L_2$ droplets should be considered as a creep flow. Diffusion interfaces around L2 embryos are produced simultaneously with droplet appearance. The velocity of a growing sphere by pure diffusion can be described by Zener's solution[32] as

$$V(r,t) = \frac{\mathrm{d}r}{\mathrm{d}t} = D\frac{c_m - c_1}{r(c_2 - c_1)}, \quad [7]$$

where $t$ is the growth time; $D$ is the diffusion coefficient; $c_m$ is the concentration of the matrix melt, which is a constant far from the diffusion interface; $c_1$ is the concentration of the liquid matrix at the diffusion interface; and $c_2$ is the concentration of the liquid droplets far from the diffusion interface. In general, the growth of the liquid droplets is controlled by diffusive or convective effects that mainly depend on the Peclet number ($Pe = Vr/D$) and Reynolds number ($Re = Vr/\mu$), where $\mu$ is the kinematic viscosity of the matrix. Substituting $V_S'$ (*i.e.*, Eq. [5]) and $D$ (which is estimated to be of the order of $10^{-8}$ to $10^{-9}$ m$^2$/s in an immiscible liquid system)[33] into $Pe$ and $Re$ showed that $Pe \ll 1$ and $Re \ll 1$; they both have a magnitude of $10^{-3}$. Based on the above description and analyses, it can be understood that pure diffusion growth can be used to describe the growth of $L_2$ droplets when $B \geq 18$ T under our experimental conditions.

### C. *Effects of an HSMF on the Formation of Droplet Arrays*

The surface of an ingot rapidly cooled to ambient temperature normally consists of equiaxed grains. Thus, it exhibits directional solidification in the radial direction. In our samples, droplet arrays formed because Rayleigh instability emerged in the surface equiaxed

grains. For the samples quenched at either 0 or 18 T, the Marangoni migration should be ascribed to the large temperature gradient. To decrease the interfacial tension, large numbers of $L_2$ droplets migrated to the higher-temperature region along the radial direction.

The temperature gradient along the radial direction decreases as the distance from the outer surface to the central axis ($s$) increases. Thus, the dispersion of the $L_2$ droplets in a grain can be divided into a planar growth stage and cellular growth stage. Figure 12 illustrates that during the planar growth stage, the real temperature distribution ($T_r$) in front of the solid–liquid interface was much larger than the local isothermal solidification temperature distribution ($T_i$) when the solidification distance was smaller than $s_1$. In this stage, the $S_1$ phase grew without constitutional supercooling. The solid–liquid interface was planar, and the droplets were dispersed in the $S_1$ phase (planar growth in Figure 12). Conversely, during the cellular stage ($s > s_1$), $T_r$ was lower than $T_i$, which resulted in constitutional supercooling. Considering the interfacial tension, the constitutional supercooling acts as a driving force. At the same time, the solid–liquid interface oscillates at a certain wavelength ($\lambda_i$), which can be written as

$$\lambda_i = 2\pi\left(\frac{D\Gamma}{V\Delta T_0}\right)^{1/2}, \qquad [8]$$

where $\Gamma = \sigma_{S_1L_2}/\Delta S$ is the Gibbs–Thomson coefficient, in which $\sigma_{S_1L_2}$ is the solid–liquid interface energy between the solid $S_1$ phase and liquid $L_2$ phase, and $\Delta S$ is the volume solidification entropy; $V$ is the growth velocity of the grain; and $\Delta T_0$ is the temperature difference between the critical temperature for the original concentration ($T_c$) and the monotectic reaction temperature also for the original concentration ($T_m$). Thus, a groove forms in the gap between the two dendrites. Then, because of the decreasing temperature gradient in front of the solid–liquid interface, Rayleigh instability occurred easily in the grooves when the system was perturbed. $\lambda_i$ of the solid–liquid interface equals $\lambda$ of the Rayleigh-type droplet arrays shown in Figures 4(a), 5(a), and 7.

For monotectic alloys, the eutectic reaction is another important feature in the phase diagram (Supplementary Figure 1). The residual $L_2$ after the monotectic reaction undergoes desolventizing decomposition and a eutectic reaction. During the desolventizing decomposition stage, Zn separates out from $L_2$. Then, the eutectic reaction occurs in the residual $L_2$. At this stage, nanoscale zinc particles separate out from $L_2$ and move along the direction of the temperature gradient. The morphology depicted in Figure 6 formed for two reasons. First, the cooling rate in the region adjacent to the wall of the quartz crucible was faster than that in the region close to the interface between the $L_2$ shell and $L_1$, which led to an increase in the diffusion distance of zinc particles along the growth direction (shown in Figure 6(d)). Second, the HSMF slows the migration of these nanoscale zinc particles. Thus, a eutectic microstructure with many dispersed nanoscale zinc particles at the initial stage and regular zinc droplet arrays at the final stage of the eutectic reaction forms along the growth direction (Figure 6(d)). This morphology and growth process are similar to those of the lamellar microstructure of a classical eutectic microstructure.

### D. *Effects of TEMF on the Evolution of the Solidified Microstructure*

Studies[10–12] have shown that TEMC induced by TEMF is generated during the solidification process of alloys under magnetic fields. In our experiments, during the bulk solidification process of the Zn-6 wt pct Bi immiscible alloy, the melt was segregated at the immiscible interval ($T_c - T_m$). The $L_2$ phase gradually sunk to the bottom of the ingot because of its greater density than that of $L_1$, whereas the upper part was mainly $L_1$. Based on the phase diagram, it can be understood that the upper Zn-rich phase is a liquid in the gap of the immiscible temperature and a solid between the monotectic temperature ($T_m$) and eutectic temperature ($T_e$, see Supplementary Figure 1) with $L_2$ under $L_1$ or $S_1$ when the melt was cooled at a slow rate. After the eutectic reaction, the $L_2$ phase solidifies into $S_2$. Therefore, there are three kinds of interfaces in the sample: the liquid–liquid ($L_1$–$L_2$) interface, the liquid–solid ($S_1$–$L_2$) interface, and the solid–solid ($S_1$–$S_2$) interface. In addition, a radial thermoelectric current ($J_{TE}$) is produced at all three interfaces because of the temperature gradient in the radial direction of the ingot (Figure 13(a)). $J_{TE}$ plays an important role in affecting the interfaces during the bulk solidification under an HSMF, and it mainly forms the $L_1$–$L_2$ and $S_1$–$L_2$ interfaces because of the Seebeck effect along the radial direction. Thus, a TEMF is generated by the interaction of $J_{TE}$ and the perpendicular HSMF at the $L_1$–$L_2$ and $S_1$–$L_2$ interfaces (Figures 13(a) and (b)). On the one hand, the flat interface of $L_1$–$L_2$ becomes concave under the action of the TEMF as a stirring force (Figure 13(a)). Because of the fluidity of the liquid phase, TEMC induced by the TEMF can only exist in the liquid phase ($L_1$ or $L_2$); it is not present in the solid phase ($S_1$ or $S_2$). If $L_1$ solidified as $S_1$ or $L_2$ solidified as $S_2$, the interface would not be changed by the TEMF. This is because the solid phase is not fluid. For this reason, the TEMF only caused the $L_1$–$L_2$ interface to form a concave shape (Figure 13(a)) and as a result, the $S_1$–$L_2$ interface also has a concave shape (Figure 13(b)). On the other hand, based on the contact angle between $S_1$, $S_2$, and the internal surface of the quartz crucible, it is concluded that the $L_2$ phase can wet the quartz crucible wall more easily than the $L_1$ phase (Figure 3(a)). The $L_1$ phase rotates in a clockwise direction ($\omega_1$) under the effect of a TEMF in $L_1$ or $S_1$ and the $L_2$ phase rotates in a counterclockwise direction ($\omega_2$) under the effect of a TEMF in $L_2$ (Figure 13(c)). Finally, the combined effect of TEMC and wettability leads to the formation of a shell-like structure under an 18-T HSMF (Figure 3(b)). After this relative rotation, the thickness of the shell becomes more uniform. In

addition, the interface between $S_2$ and $S_1$ becomes weak and contains many defects (Figures 5(b) and (d)).

The $L_2$ droplets separated out from the $L_1$ phase and a radial temperature gradient existed around the droplets in the immiscible gap. Consequently, the TEMF effect should be investigated because of the markedly different Seebeck coefficients between $L_1$ and $L_2$. To simplify the analysis, we considered that the radial temperature gradient was constant. TEMF was produced at the interface between the $L_2$ droplet and $L_1$ melt (Figure 14(a)). The TEMF in the $L_2$ droplet acted as a circumferential force, dragging the $L_2$ droplet in the circumferential direction inside the cylindrical melt. This constant force made the $L_2$ droplet move with an accelerating motion. The circumferential velocity transformed to a centrifugal force, pushing the $L_2$ droplet nearer to the $L_2$ shell, as shown in Figure 14(b). The centrifugal force can be written as

$$F_c = \frac{mv^2}{R} = \frac{3(F_M)^2 t^2}{4\pi\rho_2 R r^3} = \frac{3(B \times J_{TE})^2 t^2}{4\pi\rho_2 R r^3}, \qquad [9]$$

where $m$ is the mass of the $L_2$ droplet, $v$ is the circumferential velocity, $R$ is the distance between the $L_2$ droplet and central axis, $F_M$ represents the TEMF, and $t$ is the motion time of the droplet. Equation [9] indicates that $F_c$ increases with $F_M$ and $t$ and decreases with the radius of the $L_2$ droplet. Therefore, with the increasing cooling time and $B$, the $L_2$ droplet is pushed toward the $L_2$ shell, which increases the shell thickness. Thus, the $L_2$ droplet moves freely toward the outer surface. That is, the HSMF did not affect the droplet's centrifugal migration. Therefore, the regular centrifugal migration of Bi-rich droplets caused by the TEMF resulted in the final shell-like structure of the Zn-6 wt pct Bi immiscible alloy (Figure 5(b)).

## V. CONCLUSIONS

The effects of HSMFs on the solidification process of a Zn-Bi immiscible alloy were investigated. The following conclusions were drawn:

1. A Zn-6 wt pct Bi alloy with extremely fine Bi-rich particles (average diameter of approximately 3.8 $\mu$m) dispersed in a Zn matrix was obtained under a 29-T HSMF.
2. The refinement of the Bi-rich droplets was attributed to the magnetohydrodynamic effect. The magnetothermodynamic effect can be neglected under HSMFs of less than 29 T.
3. The Marangoni migration and, in particular, the Stokes sedimentation of the Bi-rich droplets can be suppressed by applying an HSMF. The Stokes sedimentation disappeared when the HSMF was larger than 18 T, but Marangoni migration still occurred at the edge of the sample, even when solidified under a 29-T HSMF.
4. The length and spacing of the Rayleigh-type Bi-rich particle arrays were decreased by the HSMF.
5. An HSMF can limit the coalescence in the vertical and horizontal directions, but it did not suppress the movement of a single droplet moving perpendicular to the direction of the HSMF.
6. The Bi-rich droplets grew *via* pure diffusion when $B \geq 18$ T.
7. TEMF was considered the primary reason for the regular migration of Bi-rich droplets toward the outer surface of the ingot. This regular migration resulted in the Zn-6 wt pct Bi immiscible alloy possessing a shell-like structure.

Application of an HSMF with *in situ* quenching opens up a new avenue to processing immiscible alloys with substantially decreased segregation. These experiments carried out under HSMFs offer new insights into the solidification of immiscible alloys. TEMF can be used to modify the micro- and macrostructures of immiscible alloys during their bulk solidification under magnetic fields. The solidification of alloys under a super HSMF (> 20 T) should become a new research area in the future.

## ACKNOWLEDGMENTS

The authors gratefully acknowledge the financial support from the National Key Research and Development Program of China (2016YFB0301401), the National Natural Science Foundation of Chin (U1732276, No. 51704193), and the Science and Technology Commission of Shanghai Municipality (No. 15520711000) and a General Financial Grant from the China Postdoctoral Science Foundation (No. 2017M621431). The authors also thank Natasha Lundin, Ph.D., from Edanz Group (www.edanzediting.com/ac) for editing an earlier version of this manuscript.

## OPEN ACCESS



## ELECTRONIC SUPPLEMENTARY MATERIAL

The online version of this article (https://doi.org/10.1007/s11661-018-4638-8) contains supplementary material, which is available to authorized users.

## REFERENCES

1. A. Inoue, N. Yano, K. Matsuzaki, and T. Masumoto: *J. Mater. Sci.*, 1987, vol. 22, pp. 123–31.

2. K. Uenishi, H. Kawaguchi, and K.F. Kobayashi: *J. Mater. Sci.*, 1994, vol. 29, pp. 4860–65.
3. S.H. Gelles and A.J. Markworth: *AIAA J.*, 1978, vol. 16, pp. 431–38.
4. T. Carlberg and H. Fredriksson: *Metall. Mater. Trans. A*, 1980, vol. 11A, pp. 1665–76.
5. J.Z. Zhao, H.L. Li, H.Q. Li, C.Y. Xing, X.F. Zhang, Q.L. Wang, and J. He: *Comput. Mater. Sci.*, 2010, vol. 49, pp. 121–25.
6. H. Jiang, J. Zhao, and J. He: *J. Mater. Sci. Technol.*, 2014, vol. 30, pp. 1027–35.
7. J. Zhu, T. Wang, F. Cao, H. Fu, Y. Fu, H. Xie, and T. Xiao: *J. Mater. Eng. Perform.*, 2013, vol. 22, pp. 1319–23.
8. H. Jiang, J. He, and J. Zhao: *Sci. Rep. UK*, 2015, vol. 5, p. 12680.
9. H. Yasuda, I. Ohnaka, O. Kawakami, K. Ueno, and K. Kishio: *ISIJ Int.*, 2003, vol. 43, pp. 942–49.
10. Y. Zhang, J. Gao, H. Yasuda, M. Kolbe, and G. Wilde: *Scr. Mater.*, 2014, vol. 82, pp. 5–8.
11. J.A. Shercliff: *J. Fluid Mech.*, 1979, vol. 91, pp. 231–51.
12. X. Li, Y. Fautrelle, and Z. Ren: *Acta Mater.*, 2007, vol. 55, pp. 3803–13.
13. J.K. Choi, H. Ohtsuka, Y. Xu, and W.Y. Choo: *Scr. Mater.*, 2000, vol. 43, p. 22126.
14. M. Enomoto, H. Guo, Y. Tazuke, Y.R. Abe, and M. Shimotomai: *Metall. Mater. Trans. A*, 2001, vol. 32A, pp. 445–53.
15. W. Liu, D.R. Ou, H.H. Zhou, G.Y. Tang, and F. Wu: *J. Mater. Res.*, 2001, vol. 16, pp. 2280–82.
16. H.D. Joo, J.K. Choi, S.U. Kim, N.S. Shin, and Y.M. Koo: *Metall. Mater. Trans. A*, 2004, vol. 35A, pp. 1663–68.
17. Y. Zhong, T. Zheng, L. Dong, B. Zhou, W. Ren, J. Wang, Z. Ren, F. Debray, E. Beaugnon, H. Wang, Q. Wang, and Y. Dai: *Mater. Design*, 2016, vol. 100, pp. 168–74.
18. T.X. Zheng, Y.B. Zhong, Z.S. Lei, W.L. Ren, Z.M. Ren, F. Debray, E. Beaugnon, and Y. Fautrelle: *J. Alloy Compd.*, 2015, vol. 623, pp. 36–41.
19. G. Jingjie, L. Yuan, J. Jun, S. Yanqing, D. Hongsheng, Z. Jiuzhou, and X. Xiang: *Scr. Mater.*, 2001, vol. 45, pp. 1197–1204.
20. H. Neumann, Y. Plevachuk, and F. Allenstein: *Mater. Sci. Eng. A*, 2003, vol. 361, pp. 155–64.
21. B. Majumdar and K. Chattopadhyay: *Metall. Mater. Trans. A*, 2000, vol. 31A, pp. 1833–42.
22. R.N. Grugel, T.A. Lograsso, and A. Hellawell: *Metall. Mater Trans A*, 1984, vol. 15A, pp. 1003–12.
23. B. Toloui, A.J. Macleod, D.D. Double: in *Proc Conf In Situ Composites IV*, F.D. Lemkey, H.E. Cline, and M. Melean, eds., Elsevier Science Publishing Co., New York, 1981, pp. 253–66.
24. Y. Tanimoto, H. Hayashi, S. Nagakura, H. Sakuragi, and K. Tokumaru: *Chem. Phys. Lett.*, 1976, vol. 41, pp. 267–69.
25. T. Kakeshita, K. Shimizu, S. Funada, and M. Date: *Acta Met.*, 1985, vol. 33, pp. 1381–89.
26. M. Yamaguchi and Y. Tanimoto: *Magneto Science*, Kodansha Ltd., Tokyo, 2006, pp. 3–4.
27. G. Busch and S. Yuan: *Phys. Kondens. Mater.*, 1963, vol. 1, pp. 37–66.
28. N.H. Nachtrieb: *J. Phys. Chem.*, 1962, vol. 66, pp. 1163–67.
29. S. Takeuchi and H. Endo: *Trans. Jpn. Inst. Met.*, 1961, vol. 2, pp. 243–45.
30. W. Chester: *J. Fluid Mech.*, 1957, vol. 3, pp. 304–08.
31. H. Lamb: *Hydrodynamics*, 2nd ed., Dover, New York, 1932, pp. 599–601.
32. C. Zener: *J Appl. Phys.*, 1949, vol. 20, pp. 950–53.
33. L. Ratke and S. Diefenbach: *Mater. Sci. Eng. R*, 1995, vol. 15, pp. 263–347.